

# Effective permeability of fractured porous media with power-law distribution of fracture sizes

I. I. Bogdanov,<sup>\*</sup> V. V. Mourzenko,<sup>†</sup> and J.-F. Thovert<sup>‡</sup>  
 LCD, SP2MI, BP 30179, 86962 Futuroscope Cedex, France

P. M. Adler<sup>§</sup>  
 UPMC-Sisyphé, 4 place Jussieu, Tour 56, 75252 PARIS Cedex 05, France  
 (Received 21 February 2007; published 21 September 2007)

The permeability of geological formations which contain fractures with a power-law size distribution is addressed numerically by solving the coupled Darcy equations in the fractures and in the surrounding porous medium. Two reduced parameters are introduced which allow for a unified description over a very wide range of the fracture characteristics, including their shape, density, size distribution, and possibly size-dependent permeability. Two general models are proposed for loose and dense fracture networks, and they provide a good representation of the numerical data throughout the investigated parameter range.

DOI: [10.1103/PhysRevE.76.036309](https://doi.org/10.1103/PhysRevE.76.036309)

PACS number(s): 47.56.+r, 47.11.-j, 61.43.Hv

## I. INTRODUCTION

Fractures and fracture networks strongly influence the flow properties of many geological formations, such as aquifers and oil reservoirs. Some aspects of this problem are discussed in, e.g., Sahimi [1], Adler and Thovert [2], and the National Research Council [3]. Recent advances in modeling of flow and transport phenomena in fractured rock are reviewed by Berkowitz [4]. The determination of their single-phase, steady-state effective permeability is addressed here by solving numerically the flow equations in a three-dimensional discrete description of the fracture network and of the embedding matrix.

In a series of earlier papers, various situations of increasing complexity were addressed. The connectivity of the fracture network is of course of primary importance for flow properties. Huseby *et al.* [5] investigated the geometrical and topological properties of networks of randomly located and oriented fractures, with similar sizes but possibly different shapes. A dimensionless density  $\rho'$  was introduced, which incorporates a shape factor (it is defined in the next section, along with the other quantities mentioned here). In these terms, a unique value of the percolation threshold was found to apply for a wide range of fracture shapes or mixture of shapes. This parameter was also shown to control the effective permeability of the fracture networks [6]. Later on, the influence of the matrix flow was taken into account by Bogdanov *et al.* [7]. The predominant influence of the fracture network connectivity, which is described by  $\rho'$ , was demonstrated. Note that transient compressible flow and steady-state two-phase flow were also investigated [8,9].

However, fractures in real networks have generally various sizes; such fractures are called polydisperse in contrast with monodisperse fractures which have all the same size.

The fracture size distribution often obeys a power law. The percolation of such networks was studied by Mourzenko *et al.* [10]. Again, a generalized form  $\rho'_3$  of the dimensionless density was successful in unifying the description of the percolation properties. In these terms, the critical density is nearly invariant, over a wide range of shape and size distribution parameters. Finally, Mourzenko *et al.* [11] studied the permeability of these polydisperse fracture networks. A general expression was proposed, which is the product of the volumetric surface area, weighted by the individual fracture conductivities, and of a fairly universal function of  $\rho'_3$ , which accounts for the influences of the fracture shape and size distributions.

The present work is the extension and synthesis of these earlier studies and it finally addresses the full complexity of flow in permeable fractured media, by accounting for the matrix flow and for the size polydispersity of the fractures.

The methodology follows that of Bogdanov *et al.* [7]. The flow is governed by a Darcy's equation in the rock matrix; it is also described by a two-dimensional Darcy law in the fractures, which are plane polygons randomly located and oriented in space. However, unlike in this earlier work where the fractures were assumed to be monodisperse, their sizes are distributed according to a prescribed power law. The numerical solution of the flow equations is conducted on a tetrahedral mesh which preserves and contains the fractures.

The paper is organized as follows. The geometrical model is described in Sec. II, where some geometrical notations are also introduced. In particular, a dimensionless fracture density is defined, which controls the network percolation properties. The flow problem is described in Sec. III, and the main results obtained for monodisperse fracture networks are recalled. The numerical model is presented in Sec. IV. A preliminary analysis based on earlier knowledge is conducted in Sec. V, and is used as a guideline for the discussion of the extensive set of data presented in Sec. VI, which is relative to hexagonal fractures with identical permeabilities. General models are proposed for the two regimes of loose and dense networks, in terms of two parameters only, the dimensionless fracture density and a weighted measure of the volumetric area of fractures. Then, it is shown in Secs. VII and VIII that these models also account for the influ-

<sup>\*</sup>Present address: CHLOE, Batiment IFR, rue Jules Ferry, BP 27504, 64075 Pau Cedex, France. [igor.bogdanov@univ-pau.fr](mailto:igor.bogdanov@univ-pau.fr)

<sup>†</sup>[mourzenk@lcd.ensma.fr](mailto:mourzenk@lcd.ensma.fr)

<sup>‡</sup>[thovert@lcd.ensma.fr](mailto:thovert@lcd.ensma.fr)

<sup>§</sup>[padler@ccr.jussieu.fr](mailto:padler@ccr.jussieu.fr)

ences of the fracture shapes and of the size dependence of their permeability, respectively. The main results are summarized in Sec. IX.

## II. GEOMETRICAL MODEL AND PERCOLATION PROPERTIES

Consider a permeable matrix rock, which contains a three-dimensional network of plane polygonal fractures, randomly oriented and located in space with a volumetric number density  $\rho$ . Each fracture is characterized by its surface area  $A$ , its perimeter  $P$ , and some measure  $R$  of its size, which in the following is the radius of its circumscribed disk.

According to field observations ([2], and references therein), many real probability densities of fracture sizes follow a power law such as

$$n(R) = \alpha R^{-a}, \quad (1)$$

where  $n(R)dR$  is the number of fractures with radius in the range  $[R, R+dR]$  and  $\alpha$  is a normalization coefficient. It should be emphasized that  $\alpha$  depends on  $a$ , but also on  $R_m$  and  $R_M$  which makes it a non trivial quantity (cf. [11] for precise expressions), as well as the various moments of  $R$ . In practice, the scaling exponent  $a$  ranges from 1.8 to 4.5 [12], and  $R$  varies in a large interval which can span five orders of magnitude, but it is limited by the size  $R_M$  of the largest fractures in the system and by the size  $R_m$  of the microcracks.

The flow properties of such media are investigated here in domains which widely exceed the size  $R_M$  of the largest fractures, an assumption which is not always verified in real fracture networks. Hence, for the determination of an up-scaled effective permeability, the fractured medium is approximated by a spatially periodic medium, made by the juxtaposition of identical unit cells of size  $L$  and of volume  $\tau_0$ , with  $R_m \ll R_M \ll L$ . This approximation corresponds to the classical framework of the homogenization theory (cf. [13]).

Earlier works have shown the interest of defining a dimensionless measure of the fracture density, which makes use of the concept of excluded volume in order to account for the influence of the fracture shapes. Let us first recall the definition of the excluded volume, which was introduced in the context of continuum percolation by Balberg *et al.* [14].

For a pair of objects  $F_1$  and  $F_2$ , the excluded volume  $V_{\text{ex},12}$  is the volume around  $F_1$  which would be excluded for the center of  $F_2$  if the objects were impenetrable. It can be shown [2] that if the objects are two-dimensional, convex, with areas  $A_i$ , perimeters  $P_i$  ( $i=1,2$ ), uniform random positions and uniform random orientations, the mean excluded volume is

$$V_{\text{ex},12} = \frac{1}{4}(A_1 P_2 + A_2 P_1). \quad (2)$$

For a set of identical polygons, this reduces to  $V_{\text{ex}} = AP/2$ . Anisotropic orientation distributions can easily be accounted for, as shown by Adler and Thovert [2]. For a population of objects with different shapes, a global mean excluded volume  $\langle V_{\text{ex}} \rangle$  can be obtained by averaging (2) over all the pairs in the fracture population. Generally speaking, the fractures are supposed to be statistically independent one from another.

For networks of fractures with identical sizes, but possibly different shapes, we may use  $\langle V_{\text{ex}} \rangle$  to define the dimensionless fracture density  $\rho'$ ,

$$\rho' = \rho \langle V_{\text{ex}} \rangle, \quad (3)$$

where the angle brackets  $\langle \rangle$  denote averages over the fracture population.  $\rho'$  can be interpreted as a volumetric density, since it is equal to the number of fractures per volume  $\langle V_{\text{ex}} \rangle$ ; however,  $\rho'$  also represents the mean number of intersections per fracture with other fractures in the network, and as such, it is a direct measure of the connectivity. Therefore, the definition (3) incorporates both volumetric and topological aspects.

This definition proved very successful in unifying the critical densities of networks of fractures with different shapes [5]. It was also shown that many other geometrical features, such as the volumetric density of blocks or the cyclomatic number, as well as the network permeability [6] only depend on the density  $\rho'$ .

However, percolation of polydisperse fractures (or global connectivity) is no longer controlled solely by the mean coordination, and the definition of the percolation parameter must be generalized. Since shape effects are well accounted for by  $\langle V_{\text{ex}} \rangle$ , it is useful to rewrite Eq. (2) as

$$V_{\text{ex}} = v_{\text{ex}} \frac{R_1 R_2^2 + R_1^2 R_2}{2}, \quad (4)$$

where  $v_{\text{ex}}$  is a dimensionless shape factor. Then, the definition of the dimensionless density  $\rho'$  can be generalized as

$$\rho'_3 = \rho \langle v_{\text{ex}} \rangle \langle R^3 \rangle. \quad (5)$$

The subscript is a reminder of the statistical moment of  $R$  involved in this definition. Of course,  $\rho'_3$  reduces to  $\rho'$  for monodisperse fractures.

Mourzenko *et al.* [10] have shown that the critical density  $\rho'_{3c}$  is fairly constant and equal to  $2.4 \pm 0.1$  for a wide range of fracture shapes and size distributions, and values of the exponent  $a$  in the interval  $1 \leq a \leq 4$ . A corrective term was also proposed for very elongated fracture shapes with isotropic orientations. The case of anisotropic orientations will not be addressed in this paper (see [15] for further references on this topic).

## III. FLOW EQUATIONS

The physical model in the present paper is identical to that of Bogdanov *et al.* [7]. Only its main features are recalled here. The flow in the matrix rock is described by the Darcy equations

$$\bar{\mathbf{v}} = - \frac{K_m}{\mu} \nabla P, \quad \nabla \cdot \bar{\mathbf{v}} = 0, \quad (6)$$

where  $\mu$  is the fluid viscosity,  $K_m [L^2]$  is the bulk permeability,  $\bar{\mathbf{v}}$  is the local seepage velocity in the porous matrix, and  $P$  is the pressure.

The hydraulic properties of a fracture are assumed to be quantified by a permeability  $\sigma [L^3]$ . Hence, the flow rate  $j_s$

per unit width is related to the surface pressure gradient  $\nabla_s P$  by the two-dimensional Darcy's law

$$\mathbf{j}_s = -\frac{\sigma}{\mu} \nabla_s P. \quad (7)$$

The mass conservation equation for the flow in a fracture reads

$$\nabla \cdot \mathbf{j}_s = -(\bar{\mathbf{v}}^+ - \bar{\mathbf{v}}^-) \cdot \mathbf{n}, \quad (8)$$

where  $\mathbf{n}$  is the unit vector normal to the fracture plane;  $\bar{\mathbf{v}}^+$  is the seepage velocity in the matrix on the side of  $\mathbf{n}$ , and  $\bar{\mathbf{v}}^-$  is the seepage velocity on the opposite side.

This description can account for a variety of situations, with open or partially clogged fractures [7]. In the simplest case where the fractures are regarded as open channels,  $\sigma$  is given by the classical cubic law

$$\sigma = \frac{\bar{b}^3}{12}, \quad (9)$$

where  $\bar{b}$  is some equivalent aperture. The cases where the fracture is filled by some impermeable material or its walls are clogged by some chemicals so the seepage velocity normal to the fracture induces a pressure drop are not considered here. A detailed discussion on this subject is given by Bogdanov *et al.* [7].

Note that depending on the physical origin of the fracture system as well as on its history [16–19] the fracture permeability can be size dependent. The following scaling relationship is assumed here:

$$\sigma = \sigma_0 \left( \frac{R}{R_M} \right)^\beta, \quad (10)$$

where  $\beta$  ranges from 0 to 6. The case of a variable conductivity along the fracture surface has not been addressed in the present study.

The transport equations (6)–(8) must be supplemented with macroscopic boundary conditions. As already mentioned, the fractured medium is approximated by a spatially periodic structure. Hence, when a macroscopic pressure gradient  $\nabla P$  is exerted on it, the local fields  $\bar{\mathbf{v}}$ ,  $\mathbf{j}_s$ , and  $\nabla P$  are periodic functions of the space variable  $\mathbf{r}$ . The overall seepage velocity  $\bar{\mathbf{v}}$  is defined as the volume average of the local velocities

$$\bar{\mathbf{v}} = \frac{1}{\tau_0} \left\{ \int_{\tau_m} \bar{\mathbf{v}} d\tau + \int_{S_f} \mathbf{j}_s ds \right\}, \quad (11)$$

where  $\tau_m$  is the matrix volume.  $S_f$  is the surface obtained by projecting all the fractures on their mean plane; further details are given in [6]. This flux is linearly related to the pressure gradient by an upscaled Darcy's law [2]

$$\bar{\mathbf{v}} = -\frac{1}{\mu} \mathbf{K}_{\text{eff}} \cdot \nabla P, \quad (12)$$

where  $\mathbf{K}_{\text{eff}} [L^2]$  is the effective permeability tensor of the fractured porous medium.

The upscaled permeability  $\mathbf{K}_n$  of the fracture network by itself can also be introduced. It is relevant when the matrix

contribution to the flow can be neglected and it corresponds to the steady-state effective permeability in dual porosity models. Since only isotropic fracture orientation distributions are considered here, the permeability tensors  $\mathbf{K}_{\text{eff}}$  and  $\mathbf{K}_n$  are spherical in the average, and they are simply denoted by the scalars  $K_{\text{eff}}$  and  $K_n$ . Since it does not account for the matrix permeability,  $K_n$  is always smaller than  $K_{\text{eff}}$ .

Koudina *et al.* [6] and Mourzenko *et al.* [11] studied the network permeability  $K_n$ , for monodisperse and polydisperse fracture size distributions, respectively. A general expression was proposed,

$$K_n = \rho \langle \sigma A \rangle K'_2(\rho'_3). \quad (13)$$

It successfully represents the numerical predictions in a wide range of fracture shapes (or mixture of shapes) and of the scaling exponents  $a$  and  $\beta$ .  $K_n$  involves two contributions. The dimensional term  $\rho \langle \sigma A \rangle$  is the volumetric area of fracture, weighted by the individual fracture permeabilities. The second part is a fairly universal dimensionless quantity  $K'_2(\rho'_3)$ , which accounts for the network connectivity and incorporates the effects of the fracture shape and of the fracture size distribution. Unsurprisingly, it is a function of the same quantity  $\rho'_3$  that controls the network percolation.  $K'_2$  was described by an extensive set of numerical simulation results, and by two heuristic analytic expressions, which provide good representations of these data.

Dimensionless variables denoted by a prime are defined by using three basic characteristics of the system, namely the matrix permeability  $K_m$ , a typical fracture permeability  $\sigma_0$ , and the largest fracture size  $R_M$ ,

$$R' = \frac{R}{R_M}, \quad \sigma' = \frac{\sigma}{R_M K_m}, \quad \sigma'_o = \frac{\sigma_o}{R_M K_m}, \quad K'_{\text{eff}} = \frac{K_{\text{eff}}}{K_m}, \quad (14)$$

$$K'_n = \frac{R_M}{\sigma_0} K_n.$$

#### IV. NUMERICAL MODEL

Again, the numerical implementation of the geometrical and physical models is identical to that of Bogdanov *et al.* [7], except for the size polydispersivity of the fractures, and it is described only very briefly.

The generation of the fracture network and the subsequent percolation tests are similar to those presented by Huseby *et al.* [5]. The fractures are randomly located in a cubic cell of size  $L$ , with an isotropic distribution of their normal vectors. These simplifications only provide a first approximation to the complexity of real systems where fractures tend to grow cooperatively leading to very strongly correlated structures; moreover, the fractures have a tendency to terminate against each other rather than to pass through each other. These additional features modify the macroscopic properties as discussed by [20].

Four values of the exponent  $a=1.5, 2, 2.5,$  and  $2.9$  have been considered. The cell size was generally set to  $L'=4$

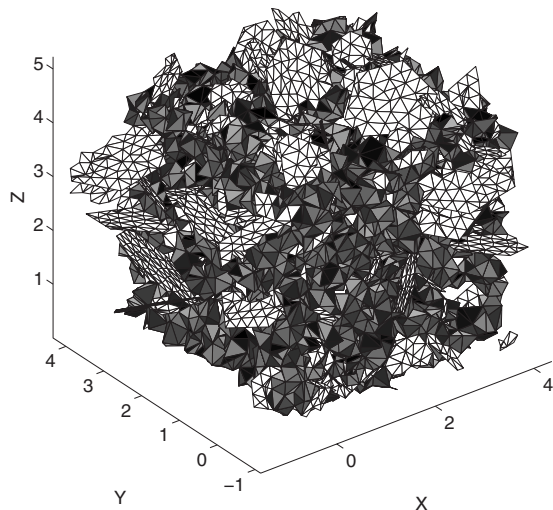


FIG. 1. An example of a tetrahedral mesh of fractured medium, with  $L'=4$  and  $\rho'_3=3.6$ . The fractures are hexagonal, with  $a=2.5$ ,  $R'_m=1/10$ , and  $\delta'=1/4$ . The sample contains 934 fractures, and the mesh is made up of about 12 000 nodes and 76 000 volume elements. The visible fractures are white.

( $L=4R_M$ ), and sometimes to  $L'=6$  or 8. The lower cutoff was  $R'_m=0.1$  ( $R_m=R_M/10$ ), or slightly larger in a few numerically demanding cases with large  $\rho$  and large  $a$ . The cell contains  $N_{fr}=\rho L^3$  fractures, which can range from a few units to about 1600 for  $a=2.9$  and  $\rho'_3=8$  with  $L'=4$ , and to almost  $10^4$  when  $a=2$  and  $\rho'_3=8$  with  $L'=8$ . An example is shown in Fig. 1.

The flow solution requires a meshing of the domain of investigation, which is conducted in two steps. The fracture network is triangulated first, with a typical edge length  $\delta$ . This is done by use of an advancing front technique, as described by Koudina *et al.* [6]. Fracture intersections are determined first and explicitly included in the mesh, with nodes along the intersection lines. Then, the matrix space between the fractures is paved by an unstructured boundary-constrained tetrahedral mesh, with the same typical edge length  $\delta$ . Again, an advancing front technique is applied, starting from the triangulated fractures. Unless otherwise stated,  $\delta=R_M/4$ ; but, small fractures with a size  $R$  of the order of  $\delta$  or smaller always contain at least four triangles. As seen in the example displayed in Fig. 1, the numbers of nodes and tetrahedra are typically of the order of  $10^4$  and  $10^5$ , respectively, when  $L'=4$ , and proportional to  $L'^3$  in the other cases. For instance, the largest mesh used in the present work ( $a=2$ ,  $\rho'_3=8$ ,  $L'=8$ ) contains 171 000 nodes and more than one million tetrahedra.

The transport coefficients  $\sigma$  and  $K_m$  can be prescribed on a per element basis (triangular surface element of fracture, tetrahedral volume element of matrix). In the present case,  $K_m$  is uniform throughout the matrix and  $\sigma$  is uniform over each fracture, although it may depend on the fracture size according to Eq. (10).

Then, the flow equations are discretized in a first-order finite volume formulation, with the control volumes centered at the mesh nodes, where the pressures are determined. The pressure gradient is assumed to be uniform over the fracture

surface elements and over the matrix volume elements. Accordingly, the flow rate is uniform in these elements and it is given by the Darcy's laws, Eqs. (6) and (7). The resulting set of linear equations is solved by the use of a conjugate gradient algorithm.

For each set of parameters,  $N_r$  random realizations of fracture networks are generated. As a rule,  $N_r=25$ ; but, this number has been reduced to 10 for large densities (generally  $\rho'_3 \geq 5$ ), because of relatively smaller statistical fluctuations of the results. Conversely, 100 realizations were used in the transition range  $1.3 \leq \rho'_3 \leq 3.6$ , where the coexistence of percolating and nonpercolating networks in the statistical set induces large fluctuations.

The influence of the mesh resolution on the accuracy of the numerical results varies according to the network density and to the fracture permeability. The errors mainly originate in the exchanges between the matrix and the fractures, around their border lines. Hence, they are minimum when the fracture network dominates the flow properties (dense networks with large  $\sigma'$ ). Conversely, they are maximum for disconnected very conducting fractures, since the fluid travels successively along the fractures and in the matrix in between. More details will be provided in Sec. VI about these different situations. Let us just mention at this point that for connected networks of very permeable fractures, the relative accuracy of the computed permeability increment  $K'_{\text{eff}}-1$  induced by the fracturation is of the order of  $\delta'_m$  or better, which is less than the statistical standard deviations when  $\delta'_m \leq 1/4$ . Therefore, for the forthcoming systematic calculations of mean effective permeabilities as functions of the fracture density, a discretization with  $\delta'_m=1/4$  was used unless otherwise mentioned; this is the best compromise between accuracy and statistical sample size, for a given computational cost.

## V. PRELIMINARY ANALYSIS

The permeabilities  $K_{\text{eff}}$  and  $K_n$  depend on a set of parameters which can be detailed as follows. First, come the fracturation characteristics, namely the three parameters of the fracture size distribution,  $a$ ,  $R_m$ , and  $R_M$ , the density  $\rho$  and the fracture shape. Then, come the transport coefficients of the matrix  $K_m$  and of the fractures  $\sigma$ , or  $\sigma_0$  and  $\beta$  for size-dependent permeabilities. This list should be completed by numerical parameters without physical meaning, such as the grid resolution  $\delta$  and the finite size  $L$  of the periodic unit cell. Their influence should of course vanish when they are set small enough (for the former) or large enough (for the latter). This paragraph can be summarized by the relations

$$K_{\text{eff}}, K_n = f(a, R_m, R_M, \rho, \text{shape}, K_m, \sigma_0, \beta, L, \delta). \quad (15)$$

However, earlier works cited in Secs. II and III concluded that the influence on the percolation and flow properties of the network of all the geometrical parameters can be summarized by a single dimensionless density  $\rho'_3$ , in addition to the dimensional prefactor in Eq. (13). Therefore, we may expect the dimensionless permeabilities  $K'_n$  and  $K'_{\text{eff}}$  to depend on the following physical dimensionless parameters, in addition to the artificial numerical ones:

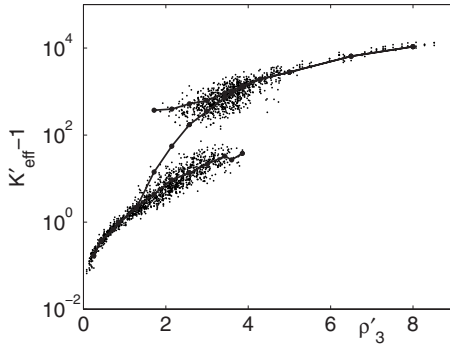


FIG. 2. The dimensionless permeability increment  $K'_{\text{eff}}-1$  for permeable media containing hexagonal fractures with  $a=2$ ,  $\beta=0$ ,  $\sigma'=10^4$ ,  $R'_m=1/10$ ,  $L'=4$ , and  $\delta'=1/4$ . Dots are individual data per realization and per flow direction. The lines join the averages of the data, global per density, separately for percolating and nonpercolating networks.

$$K'_n = f_1(\rho'_3, \mathcal{S}, L', \delta'), \quad K'_{\text{eff}} = f_2(\rho'_3, \mathcal{S}, \sigma'_0, L', \delta'), \quad (16)$$

where

$$\mathcal{S} = \rho R_M \frac{\langle \sigma' A \rangle}{\sigma'_0} \quad (= \rho R_M \langle A \rangle \text{ when } \beta = 0) \quad (17)$$

and

$$L' = L/R_M, \quad \delta' = \delta/R_M. \quad (18)$$

The forthcoming results will be discussed in these terms. Note that  $\mathcal{S}$  is a measure of the volumetric area of fracture in the medium, weighted by the permeability of the individual fractures.

Analytical results can be obtained in two asymptotic cases, and used as guidelines for the discussion. Consider first the limiting case of a very dilute fracture network. The fractures are not connected, and their independent contributions to the permeability increase can be summed up. Since each of these contributions is proportional to the cubed size of the corresponding fracture, the leading order term in the expansion of  $K'_{\text{eff}}$  is proportional to the third moment  $\langle R^3 \rangle$  of the size distribution, or in other words, for given fracture characteristics, to the density  $\rho'_3$ ,

$$K'_{\text{eff}} = 1 + \kappa \rho'_3 + O(\rho'^2_3) \quad (\rho'_3 \ll 1). \quad (19)$$

This is the classical form of a virial expansion, such as the Maxwell's formula for the conductivity of a material which contains noninteracting spherical inclusions [21]. For circular, randomly oriented superconducting fractures ( $\sigma' \rightarrow \infty$ ), this yields (see for instance, [7,22])

$$\kappa = \frac{32}{9\pi^2} \approx 0.360 \quad (\text{disks, } \sigma' = \infty). \quad (20a)$$

More generally, for ellipses with an aspect ratio  $f$ , it can be deduced from the general solution for a superconducting ellipsoidal inclusion [23] that

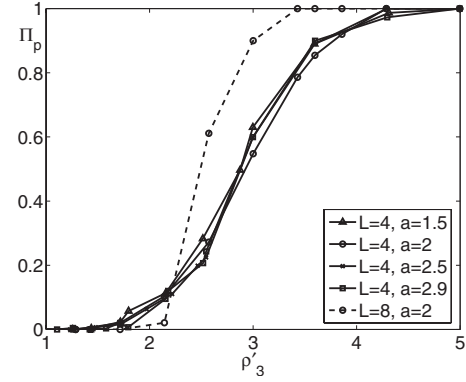


FIG. 3. The fraction  $\Pi_p$  of percolating networks versus  $\rho'_3$ , for hexagonal fractures with  $a=1.5$  ( $\Delta$ ),  $2.0$  ( $\circ$ ),  $2.5$  ( $\times$ ), and  $2.9$  ( $\square$ ).  $L'=4$  (solid lines) or  $8$  (broken line).  $R'_m=1/10$ , except for  $R'_m=1/8$  when  $(\rho'_3 > 2.5, a=2.5)$  or  $(\rho'_3 > 1.72, a=2.9)$ , and  $R'_m=0.15$  when  $(\rho'_3 > 4.5, a=2.9)$ .

$$\kappa = \frac{2e^4}{9f[K(e) - E(e)][E(e) - f^2K(e)]} \quad (\text{ellipses, } \sigma' = \infty), \quad (20b)$$

where  $e = \sqrt{1-f^2}$  and  $K$  and  $E$  are the complete elliptic integrals of the first and second kind, respectively.

It seems that no analytical solution could be derived for other fracture shapes, but Mansfield *et al.* [24] provide a set of numerical results for regular polygons with three to eight vertices, from which the coefficient  $\kappa$  in (19) can be obtained. It never departs by more than 4% from its value (20a) for disks.

There is no result in the literature for fractures with finite permeabilities, but again, as the sum of independent contributions of individual fractures proportional to their cubed size, the first-order term would be proportional to  $\langle R^3 \rangle$  and therefore to  $\rho'_3$ .

In the opposite limit of very dense fracture networks, when the fractures are highly interconnected and their whole surface contributes to the flow, the effective permeability can be deduced from the result of [25] for infinite plane fractures. This yields in the case of an isotropic orientation distribution (see Mourzenko *et al.* [11])

$$K'_{\text{eff}} = 1 + \frac{2}{3} \sigma'_0 \mathcal{S}, \quad \rho'_3 \gg 1. \quad (21)$$

Here, the main parameter is the volumetric fracture area, which involves the second moment  $\langle R^2 \rangle$  of the fracture sizes. This result should apply in the limit of very dense networks, regardless of the fracture shapes. Note also that the volumetric area is the most accessible characteristic of a fracture network, from a trace map or even from a mere line survey [26].

Several transition regimes should take place between these two limiting cases of totally unconnected or interconnected fractures. First, when  $\rho'_3$  increases from zero, second- and higher-order corrections to Eq. (19) should progressively become significant. Then, a sharp transition should take place when  $\rho'_3$  increases beyond the critical density at which

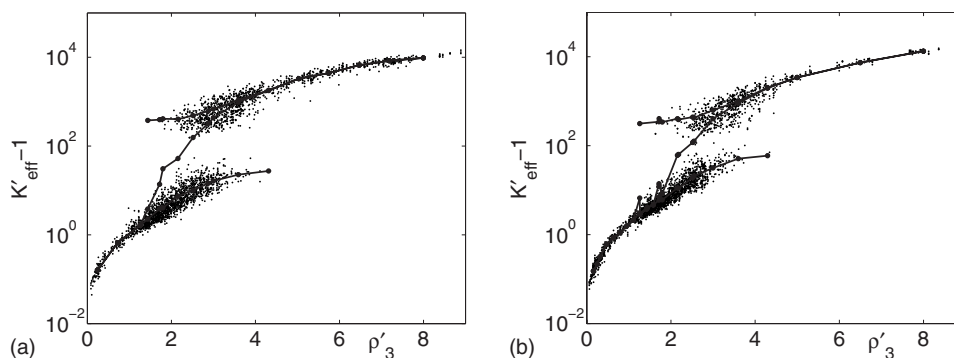


FIG. 4. Dimensionless permeability increment  $K'_{\text{eff}}-1$  for permeable media containing hexagonal fractures with exponents  $a=1.5$  (a) and  $2.9$  (b). The other parameters are identical to those in Fig. 2, except in (b) for  $R'_m=1/8$  when  $\rho'_3 > 1.72$  and  $R'_m=0.15$  when  $\rho'_3 > 4.5$ . Same conventions as in Fig. 2. See also Fig. 2 for  $a=2.0$  and Fig. 5(d) for  $a=2.5$ .

the fracture networks start percolating, especially when  $\sigma' \gg 1$ , since the permeability  $K_n$  of the network by itself suddenly switches from zero to a finite value. Finite size effects, i.e., an influence of the artificial parameter  $L$  in the numerical model, can be expected in this situation. Since  $\rho'_3$  is known to control the percolation of the fracture network, it is expected to remain a crucial parameter far beyond the range of Eq. (19). Finally, for large  $\rho'_3$ , when the flow in the fracture network dominates,  $K'_{\text{eff}}$  should be close to  $1 + \sigma' K'_n$ , with the network permeability  $K_n$  modeled by Eq. (13). Eventually, for even larger fracture densities,  $K'_{\text{eff}}$  should approach the limit (21).

An extensive set of results is presented first in the next section, for hexagonal fractures with identical permeabilities ( $\beta=0$ ), and discussed in relation with the previous analysis. Then, it will be shown in Secs. VII and VIII that the formulation in terms of the dimensionless parameters  $\rho'_3$  and  $\mathcal{S}$  can also account for the fracture shape and the exponent  $\beta$ .

## VI. RESULTS FOR HEXAGONAL FRACTURES WITH $\beta=0$

### A. Preliminary overview

Before considering specific situations, let us give an overview of the typical trends. Fractured media were generated for a set of target densities  $\rho'_3$  up to 8. Data for hexagonal fractures, with  $a=2$ ,  $\beta=0$ ,  $\sigma'=10^4$ ,  $R'_m=1/10$ ,  $L'=4$ , and  $\delta'=1/4$  are given in Fig. 2. The number of network realizations depends on the range of the density  $\rho'_3$ :  $N_r=25$  for  $\rho'_3 < 1.3$  and for  $3.6 < \rho'_3 < 5$ ;  $N_r=100$  for  $1.3 \leq \rho'_3 \leq 3.6$ ;  $N_r=10$  for  $\rho'_3 \geq 5$ . Since the flow calculations have been conducted along the  $x$ ,  $y$ , and  $z$  directions, the number of data is  $3N_r$ .

The individual effective permeabilities, per realization and per direction are given in Fig. 2 as functions of the actual density  $\rho'_3$  of the generated fracture networks, together with their statistical averages. Separate averages for percolating and nonpercolating fracture networks are also shown in the figure, which make clear that a gradual transition takes place between two branches in a range of intermediate densities.

The fraction  $\Pi_p$  of percolating networks is plotted in Fig. 3 as a function of  $\rho'_3$ . It switches from zero to one when the

density increases from  $\rho'_3 \approx 2$  to  $\rho'_3 \approx 4$ . Note that nearly identical curves are obtained for other values of  $a$  ranging from 1.5 to 2.9, which illustrates that the dimensionless density  $\rho'_3$  summarizes very efficiently the influence of the size distribution on the percolation properties of fracture networks, as already demonstrated by Mourzenko *et al.* [10]. The width of this transition region is of course size dependent, and it decreases as  $L'$  increases. This is clearly shown in Fig. 3 by the additional data for  $L'=8$  which will be discussed in Sec. VI D.

In the following, the word “loose” packing refers to the density range where  $\Pi_p \approx 0$ , as opposed to dense packings, when  $\Pi_p \approx 1$ . These two ranges are separated by the transition region.

Figure 4 provides the counterparts of Fig. 2 for the exponents  $a=1.5$  and  $2.9$  [see also Fig. 5(d) for  $a=2.5$ ]. The other parameters are unchanged, except for  $R'_m$  which is slightly larger in some of the most demanding cases, when both  $a$  and  $\rho'_3$  are large. Very similar pictures are obtained in all cases.

Figure 5 presents data for  $a=2$  and for  $\sigma'$  ranging between 10 and  $10^4$ . All other parameters are kept identical to those in Fig. 2. The large ratio (about 100 when  $\rho'_3 \approx 3$ ) observed in Fig. 4 between the two branches for percolating and nonpercolating networks when  $\sigma'=10^4$ , rapidly diminishes for smaller  $\sigma'$ . This ratio is about 10 when  $\sigma'=10^3$ , and it increases up to about 100 when  $\sigma'=10^2$ ; the difference nearly vanishes for  $\sigma' \leq 10$ . Plots similar to Fig. 5 for other values of the exponent  $a$  (not shown here) display exactly the same features.

It is interesting to note that fractures with  $\sigma'$  of the order of 10, with a density in the transition range  $2 \leq \rho'_3 \leq 4$ , have the same impact on the fractured medium effective permeability, whether they constitute a percolating network or not. This feature was already noticeable in Figs. 6 and 8 of Bogdanov *et al.* [7] for monodisperse fracture networks, although it was not stressed in the discussion.

Let us now examine more closely particular situations which correspond to various ranges of fracture density.

### B. Dilute limit

As discussed in Sec. V, a small concentration of fractures induces a permeability increment which is proportional to

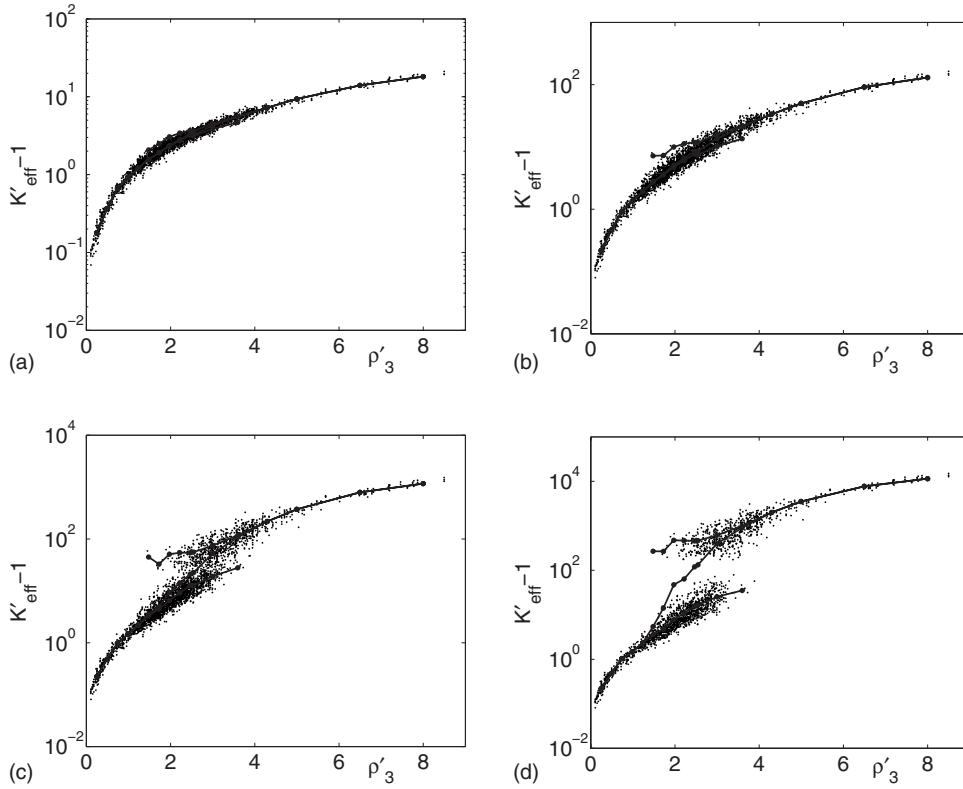


FIG. 5. Dimensionless permeability increment  $K'_{\text{eff}}-1$  for permeable media containing hexagonal fractures with  $a=2.5$  and  $\sigma' = 10$  (a),  $10^2$  (b),  $10^3$  (c), and  $10^4$  (d). The other parameters are identical to those in Fig. 2, except for  $R'_m = 1/8$  when  $\rho'_3 > 2.5$ . Same conventions as in Fig. 2.

the concentration [Eq. (19)]. The coefficient  $\kappa$  depends both on the fracture shape and on their permeability  $\sigma'$ . Since the dependence on the shape is investigated in Sec. VII, only hexagonal fractures are considered in this section, over the whole range of  $\sigma'$ .

In the dilute limit, there is no hydraulic interactions between the fractures. The disturbances that they induce in the flow pattern with respect to the flow in the intact matrix can be evaluated independently, and the corresponding contributions to the permeability increase can be simply summed up. If a very large volume  $\Omega$  contains  $N$  identical randomly oriented fractures, the upscaled Darcy's law (12) reads

$$\bar{\mathbf{v}} = -\frac{1}{\mu} \left( K_m + \frac{1}{\Omega} \sum_{i=1}^N \mathbf{k}_i \right) \cdot \bar{\nabla} P. \quad (22)$$

The fracture contributions  $\mathbf{k}_i$  are all random rotations, according to the fracture orientations, of a tensor of the form

$$\mathbf{k} = \begin{pmatrix} k_{\parallel} & 0 & 0 \\ 0 & k_{\parallel} & 0 \\ 0 & 0 & k_{\perp} \end{pmatrix}, \quad (23)$$

where  $k_{\parallel}$  and  $k_{\perp}$  correspond to the directions parallel and normal to the fracture plane, respectively.

In the limit of large  $N$ , the summation in Eq. (22) can be replaced by the statistical average  $\rho\langle\mathbf{k}_i\rangle$  which is a spherical tensor, since the fracture orientations are isotropically distributed. Furthermore, all the tensors  $\mathbf{k}_i$  have the same trace  $2k_{\parallel}+k_{\perp}$ , and this applies also to their average.

Hence, the determination of the coefficient  $\kappa$  in Eq. (19) only requires the knowledge of the trace of the tensor  $\mathbf{k}$ , which represents the influence of a single fracture in an infinite medium. As discussed in Sec. V,  $\mathbf{k}$  is known analytically in a few simple cases, when  $\sigma' = \infty$ . It can be calculated numerically in other situations, by considering a single fracture in a domain large enough to be regarded as unbounded. In practice, a single fracture was put in a unit cell with spatially periodic boundary conditions. Preliminary calculations showed that the data for  $L'=6$  were very close to the ones with  $L'=4$ , and the results in a few cases for  $L'=6$  and  $L'=8$  were found identical. Therefore, the systematic data presented in the following were obtained for  $L'=6$ .

The ratio  $(K'_{\text{eff}}-1)/\rho'_3$ , which corresponds to the coefficient  $\kappa$  in Eq. (19), is plotted as a function of  $\sigma'$  in Fig. 6. The data are obtained with various mesh resolutions  $\delta'_m = 1/4, 1/8, \text{ and } 1/16$ , and they are extrapolated to  $\delta'_m \rightarrow 0$ .

Significant discretization errors of the order of  $2\delta'$  are observed when  $\sigma' \gg 1$ . Various tests show that the flow around the fracture edges is not accurately calculated. Hence, the most efficient improvement of the results would not result from a refinement of the mesh in the fractures, but instead in the matrix near their edges. In practice, the fractures behave as if their radii were increased by  $\delta/2$ . For moderate  $\sigma'$ , the relative error decreases, and it never exceeds a few percent when  $\sigma' < 1$ .

The coefficient  $\kappa$  is found nearly constant when the fracture permeability is larger than 10, and equal to the coefficient  $\kappa_{\infty}$  for superconducting fractures. The extrapolated value 0.335 obtained for  $\sigma' = 10^4$  is 4% smaller than the result  $\kappa_{\infty} = 0.349$  of Mansfield *et al.* [24]. For less permeable fractures,  $\kappa$  decreases, and ultimately becomes proportional

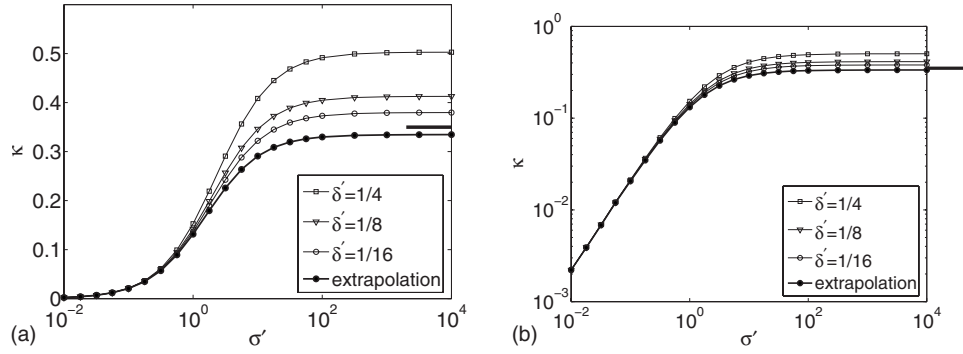


FIG. 6. The coefficient  $\kappa = (K'_{\text{eff}} - 1)/\rho'_3$  in Eq. (19) for dilute dispersions of hexagonal fractures, as a function of the fracture permeability  $\sigma'$ . Semilog (a) and log-log (b) scales. The data have been obtained with  $\delta' = 1/4$  ( $\square$ ),  $1/8$  ( $\nabla$ ), and  $1/16$  ( $\circ$ ), and by extrapolating toward  $\delta' \rightarrow 0$  ( $\bullet$ ). The horizontal mark at  $\sigma' = 10^4$  is the result of Mansfield *et al.* [24] for  $\kappa_\infty$ .

to  $\sigma'$ . These variations are well described by the following empirical expression:

$$\kappa = \frac{\sigma'}{\sigma' + 3/2} \kappa_\infty. \quad (24)$$

A comparison of this model with the numerical data is provided in Fig. 7, where the ratio  $\kappa/\sigma'$  is plotted as a function of the dimensionless fracture permeability. The data are slightly scattered for the very small values of  $\sigma'$ , probably because the permeability increment is so small that accumulated round-off errors start influencing the results.

### C. Small densities

When the fracture density increases, it can be expected that additional terms play a role in the expansion (19), because the perturbations in the flow pattern due to the individual fractures interact, and also because some of the fractures are connected. Recall that for a monodisperse network  $\rho'_3$  is exactly the mean number of intersections per fracture, and that for polydisperse networks it is also a measure of the connectivity.

Numerical data for polydisperse networks, with various exponents  $a$ , moderate densities  $\rho'_3$  and  $\sigma' = 1, 10, \text{ and } 100$ ,

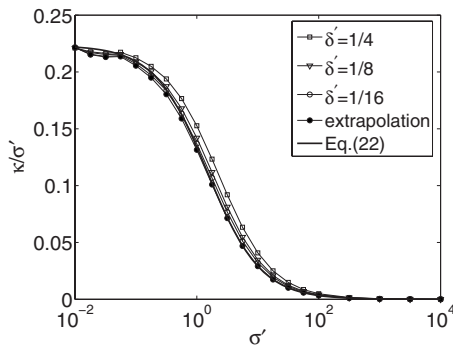


FIG. 7. The coefficient  $\kappa/\sigma'$  for dilute dispersions of hexagonal fractures, as a function of the fracture permeability  $\sigma'$ . Data are for  $\delta' = 1/4$  ( $\square$ ),  $1/8$  ( $\nabla$ ), and  $1/16$  ( $\circ$ ), and  $\delta' \rightarrow 0$  ( $\bullet$ ). The thick solid line is the model (24).

are compared in Fig. 8 to a simple generalization of (19) which includes a quadratic term

$$K'_{\text{eff}} = 1 + \kappa\rho'_3 + \kappa^2\rho'^2_3, \quad (25)$$

where  $\kappa$  is deduced from Eq. (24) with  $\kappa_\infty = 0.335$ . The occurrence of the same coefficient in the first- and second-order terms is fortuitous. The data for  $\sigma' > 100$  are not displayed, because they are nearly identical to that for  $\sigma' = 100$ . Since the numerical data have been obtained with  $\delta' = 1/4$ , the discretization errors can be significant, especially when  $\sigma'$  is large. Instead of correcting them as done in Figs. 6 and 7 by extrapolating to  $\delta' \rightarrow 0$ , they are plotted in Fig. 8 versus a modified density  $\rho'_{3,\text{app}}$  which accounts for the larger apparent size  $R + \delta/2$  of the fractures.

Equation (25), which involves a single parameter  $\kappa_\infty$ , is seen to be fairly successful in representing the permeability of moderately fractured media for  $\rho'_3 < 2$ , i.e., when the fracture networks never percolate. This result will be generalized in Sec. VII for other fracture shapes.

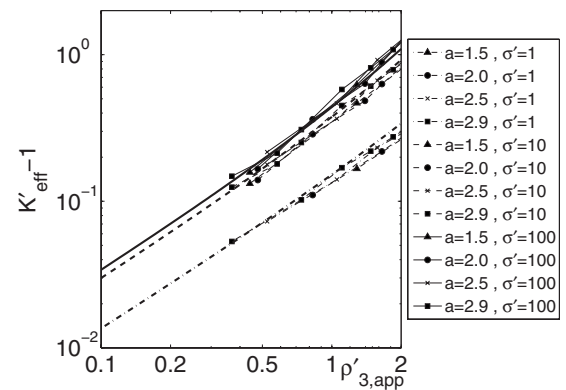


FIG. 8. The mean dimensionless permeability increment  $K'_{\text{eff}} - 1$  for permeable media containing hexagonal fractures as a function of  $\rho'_3$ . Data are for  $a = 1.5$  ( $\triangle$ ),  $2$  ( $\circ$ ),  $2.5$  ( $\times$ ), and  $2.9$  ( $\square$ ), and for  $\sigma' = 1$  (dashed-dotted lines),  $10$  (dashed lines), and  $100$  (solid lines). The heavy lines are the model (25). The network density  $\rho'_{3,\text{app}}$  is corrected in order to account for the discretization effects.

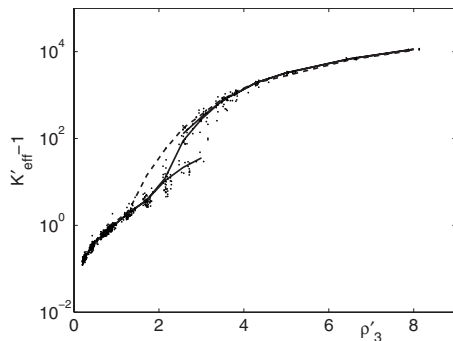


FIG. 9. The dimensionless permeability increment  $K'_{\text{eff}}-1$  for permeable media containing hexagonal fractures with  $a=2$ ,  $\beta=0$ ,  $\sigma'=10^4$ ,  $R'_m=1/10$ , and  $L'=8$ . Same conventions as in Fig. 2. The broken line is the mean  $\langle K'_{\text{eff}}-1 \rangle$  when  $L'=4$  (see Fig. 2).

#### D. Transition range

As already mentioned, when  $L'=4$ , the percolation probability  $\Pi_p$  of the networks progressively increases from zero to one in the range of density  $\rho'_3=2-4$ , for  $1.5 \leq a \leq 2.9$  (Fig. 3). When a spanning cluster of fractures exists, it constitutes a preferential path which dominates the flow properties of the fractured medium when the fracture permeability  $\sigma'$  is large. Accordingly, two branches separated by nearly two decades exist in the curves in Figs. 2 and 4 for the effective permeability averaged either over the percolating or over the nonpercolating networks. Recall however that the separation between the two branches decreases for less permeable fractures, and nearly vanishes when  $\sigma' \leq 10$  (Fig. 5). Hence, a real transition occurs only for very large  $\sigma'$ , as for networks of resistive bonds (see the classical calculations of [27]).

On the other hand, the range of density over which the transition takes place depends on the system size, as is well known from percolation theory [28]. The coexistence of percolating and nonpercolating networks in a statistical set with the same density is a finite-size effect. The width  $\Delta$  of the transition region decreases as  $L'$  increases, and ultimately, when  $L' \rightarrow \infty$ ,  $\Pi_p$  switches abruptly from zero to one when  $\rho'_3$  reaches the percolation threshold  $\rho'_{3c}$ . Not only  $\Delta$  depends on the system size, but also the density for which the percolation probability is 0.5. Mourzenko *et al.* [10] found it equal to about 2.9 and 2.6 for  $L'=4$  and 8, respectively, and it converges to the percolation threshold  $\rho'_{3c}=2.4$  when  $L'$  further increases.

All these effects are illustrated in Figs. 3 and 9, where data for  $L'=8$  are compared to those for  $L'=4$ , when  $a=2$ . The transition of the percolation probability from 0 to 1 is indeed steeper, and  $\Pi_p$  reaches 1/2 for  $\rho'_3 \approx 2.6$  instead of 2.9 (Fig. 3). Accordingly, when  $\sigma' \gg 1$ , the transition of the mean effective permeability  $K'_{\text{eff}}$  takes place in a narrower range of densities (Fig. 9).

However, out of the transition range  $2.1 \leq \rho'_3 \leq 3$ , the mean permeabilities are identical for  $L'=4$  and 8, which shows that the data are not affected anymore by any finite size effects. For moderate  $\sigma'$ , when two branches could not be distinguished in Fig. 5, identical results for  $\langle K'_{\text{eff}} \rangle$  are obtained with  $L'=4$  and 8, over the whole range of fracture densities (not displayed here).

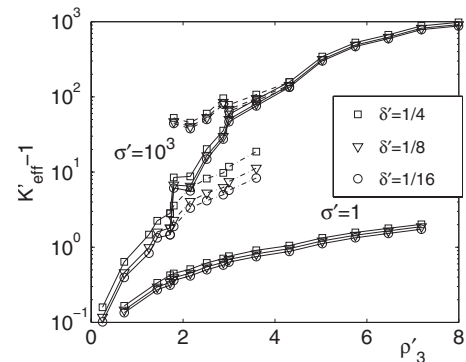


FIG. 10. The dimensionless permeability increment  $K'_{\text{eff}}-1$  for permeable media containing hexagonal fractures with  $a=1.5$ ,  $\beta=0$ ,  $\sigma'=1$  or  $10^3$ ,  $R'_m=1/10$ ,  $L'=4$  and  $\delta'=1/4$  ( $\square$ ),  $1/8$  ( $\nabla$ ), and  $1/16$  ( $\circ$ ). The data are averages over 10 realizations. In the case of  $\sigma'=10^3$ , the separate averages over the percolating and nonpercolating cases are also shown.

#### E. Dense networks

Before proceeding any further, it is necessary to complete the discussion of the numerical discretization effects, which was sketched in Sec. IV and developed in more detail in Sec. VI B for the dilute case. An illustrative set of results is presented in Fig. 10 for fracture networks with a scaling exponent  $a=1.5$ . The calculations have been conducted with  $\delta'=1/4, 1/8$ , and  $1/16$ , and with  $\sigma'=1$  and  $10^3$ .

When  $\sigma'=1$ , the various discretization parameters yield three curves which are slightly shifted vertically. By comparing with an extrapolation toward  $\delta' \rightarrow 0$ , the numerical error is found of the order of  $\delta'$  or better, whatever  $\rho'_3$ .

The situation is different when  $\sigma' \gg 1$ , since different behaviors are observed for percolating and nonpercolating networks. For percolating networks, the relative error is found again better than  $\delta'$ . It can be significantly smaller when  $\rho'_3$  and  $\sigma'$  are large, i.e., when fracture flow truly dominates the effective permeability. Larger errors, of the order of  $2\delta'$ , occur in the low density range, which are discussed in Sec. VI B.

The poorest accuracy is observed in the transition range, for nonpercolating networks. The permeabilities calculated with  $\sigma'=2$  can be overestimated by a factor of 2. This can be understood when it is recalled that the errors are mostly due to the exchanges between the fracture edges and the matrix. A fracture network in a subcritical state contains many relatively large, but unconnected clusters, and the effective permeability is controlled by the gaps which the fluid must cross when hopping from a very conducting fracture cluster to the next one, through the regions where the description is the least accurate.

However, the lesser performances of the numerical code in this particular situation are not very important, for at least two reasons. First, as discussed in Sec. VI D, the existence of a wide transition range is a consequence of the limited size of the numerical samples. On the other hand, in this region, the main criterion is whether the network percolates, in which case the permeability is large and correctly evaluated, or not, in which case the permeability is much smaller. In

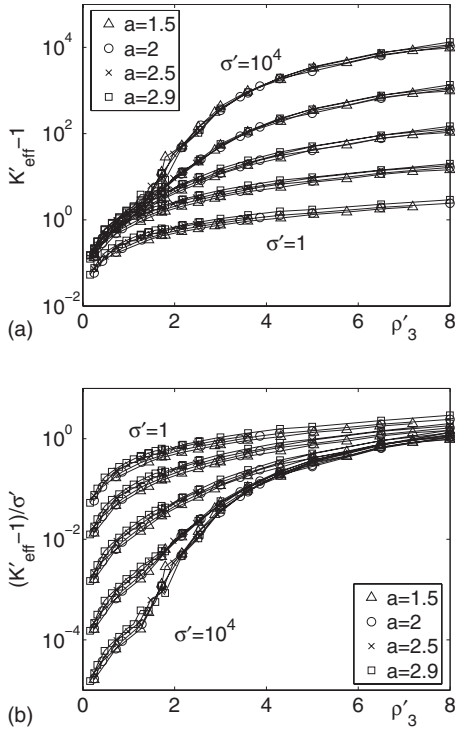


FIG. 11. The mean dimensionless permeability increment for permeable media containing hexagonal fractures as functions of  $\rho'_3$ .  $K'_{\text{eff}} - 1$  is shown in (a) and  $(K'_{\text{eff}} - 1)/\sigma'$  is shown in (b). Data are for  $L'=4$ ,  $a=1.5$  ( $\Delta$ ), 2 ( $\circ$ ), 2.5 ( $\times$ ), and 2.9 ( $\square$ ), and for  $\sigma' = 1-10^4$  [bottom to top in (a), and bottom to top in (b)].

particular, the actual value of  $K_{\text{eff}}$  for the nonpercolating networks has a very small impact over the statistical average which is dominated by the percolating ones and their probability  $\Pi_p$  of occurrence.

All in all, the uncertainty of the results presented in this paper, which is generally of the order of  $\delta'$ , should always be compared with the huge variations of the effective permeability, which span several orders of magnitude. Therefore, this uncertainty has little practical consequence.

When the probability of percolation is close to one, a preferential flow path through the fractures nearly always exists. Its permeability has been studied by Mourzenko *et al.* [11]. When  $K_n$  widely exceeds  $K_m$ , it dominates the effective permeability of the fractured medium. This may occur either because  $\sigma' \gg 1$ , even for a moderate density  $\rho'_3$ , or because the fracturation is very dense, even if  $\sigma'$  is moderate. Since  $K_n$  is proportional to the fracture permeability,  $K'_{\text{eff}} - 1$  should be proportional to  $\sigma'$ . More precisely, in this limit, the effective permeability is expected to converge toward

$$K'_{\text{eff}} \approx 1 + \sigma' K'_n \quad (K_n \gg K_m). \quad (26)$$

This trend is confirmed in Fig. 11, where the increments  $K'_{\text{eff}} - 1$  obtained for networks of hexagonal fractures with various exponents  $a$  and  $\sigma'$  ranging from 1 to  $10^4$  are plotted as functions of  $\rho'_3$ . The data in Fig. 11(a) are mostly influenced by  $\sigma'$ , whereas they tend to converge toward a common asymptote in Fig. 11(b), where  $K'_{\text{eff}} - 1$  is normalized by  $\sigma'$ . The curves for  $(K'_{\text{eff}} - 1)/\sigma'$  are close together as soon as

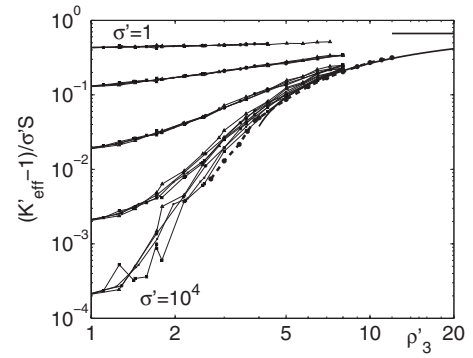


FIG. 12. The normalized mean permeability increments  $(K'_{\text{eff}} - 1)/\sigma' S$  for permeable media containing hexagonal fractures as functions of  $\rho'_3$ . Data are for  $L'=4$ ,  $a=1.5$  ( $\Delta$ ), 2 ( $\circ$ ), 2.5 ( $\times$ ), and 2.9 ( $\square$ ), and  $\sigma' = 1-10^4$  (bottom to top). The solid curve is the model (28) for  $K'_2$  and the straight line corresponds to Eq. (21). The broken line (---) corresponds to  $\sigma' K'_n$  obtained by Mourzenko *et al.* [11] for  $a=2.9$ .

$\rho'_3 \geq 4$ , when  $\sigma' \geq 100$ . For less permeable fractures, a larger density is required to reach this regime. For instance, for  $\sigma' = 10$ ,  $\sigma' K'_n$  is of the order of a few units when  $\rho'_3 = 8$  and for this value the curves for  $(K'_{\text{eff}} - 1)/\sigma'$  join with the curves for larger  $\sigma'$ .

Mourzenko *et al.* [11] found that the network permeability  $K_n$  is proportional to the volumetric area  $S$  of fractures. When Eq. (13) is introduced into (26), it yields

$$K'_{\text{eff}} \approx 1 + \sigma' S K'_2(\rho'_3). \quad (27)$$

A direct comparison of the numerical data for  $(K'_{\text{eff}} - 1)/\sigma' S$  is made in Fig. 12 with an analytical expression which provides a good approximation of  $K_n$  [11],

$$K'_2 = \frac{2}{3} \left( 1 - \frac{10}{\rho'_3 + 6.6} \right). \quad (28)$$

This model clearly captures the trend of the effective permeability of the fracture medium when the fracture flow is predominant. For comparison, some data of Mourzenko *et al.* [11] for  $K_n$  in the case of  $a=2.9$  are recalled in Fig. 12.

It was not possible to reach computationally the regime where  $K'_{\text{eff}}$  is governed by Eq. (22), which seems to require  $\rho'_3 > 20$ , but nevertheless, this expression is a likely asymptote for the numerical data, for all exponents  $a$  and all fracture permeabilities  $\sigma'$ , as shown by Fig. 12. Note that the model [(13) and (28)] reduces to (21) when  $\rho'_3 \rightarrow \infty$ .

It can also be noticed that the normalization by  $S$  totally eliminates the slight vertical shift between the curves in Fig. 11 with identical  $\sigma'$ , but different exponents  $a$ . Recall that  $\langle \sigma A \rangle$  in Eq. (13) involves the moment  $\langle R^2 \rangle$  instead of  $\langle R^3 \rangle$  which is incorporated in  $\rho'_3$ . The plot in Fig. 12 shows that the influence of this second geometrical parameter, and more generally of the fracture size distribution, is well accounted for by the decomposition (27), even when the matrix significantly or predominantly contributes to  $K_{\text{eff}}$ . Hence, the general dependence (16) can be written as

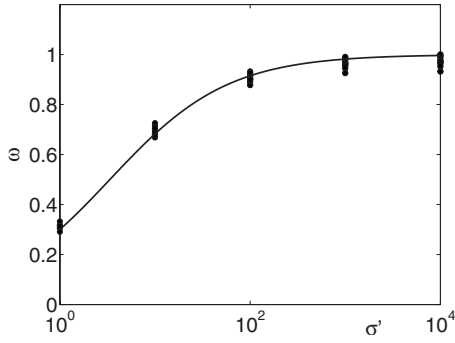


FIG. 13. The ratio  $\omega$  [see Eq. (30)] as a function of  $\sigma'$ . The symbols are the same numerical data as in Fig. 12, for all values of  $a$  and  $\rho'_3 \geq 4$ . The line is the model (31).

$$K'_{\text{eff}} = 1 + \sigma' S K''_2(\rho'_3, \sigma'), \quad (29)$$

where  $K''_2(\rho'_3, \sigma')$  reduces to  $K'_2(\rho'_3)$  when the network permeability dominates. Recall that the domain size  $L'$  which appears in the argument list in (16) does not play any role in the dense regime when  $L' \geq 4$ , as shown in Sec. VI D.

The form of  $K''_2$  can be investigated by considering the gradual transition which seems to take place for large densities between a permeability increment  $K'_2$  for large  $\sigma'$  and a permeability increment  $2/3$  for small  $\sigma'$ . It can be quantified by the ratio  $\omega$ ,

$$\omega = \frac{\frac{2}{3} - \frac{K'_{\text{eff}} - 1}{\sigma' S}}{\frac{2}{3} - K'_2}. \quad (30)$$

This ratio is plotted in Fig. 13. All the numerical data with  $\rho' \geq 4$  presented in Fig. 12 are displayed, and they are seen to gather remarkably onto a single curve, regardless of the density  $\rho'_3$  and of the exponent  $a$ . A heuristic, but successful model for these data can be proposed as

$$\omega \approx \frac{1}{1 + \frac{7}{3} \sigma'^{-0.7}}. \quad (31)$$

Eventually, the permeability increment  $K''_2$  in (29) induced by fractures in a permeable medium is given by

$$K''_2(\rho'_3, \sigma') = \frac{2}{3} - \omega(\sigma') \left( \frac{2}{3} - K'_2(\rho'_3) \right) \approx \frac{2}{3} - \frac{\frac{2}{3} - K'_2(\rho'_3)}{1 + \frac{7}{3} \sigma'^{-0.7}} \quad (32)$$

$$(\rho'_3 \geq 4).$$

This formula is valid for all the cases previously investigated, as soon as the density is large enough. Its predictions are directly compared to the numerical data in Fig. 14, and an excellent agreement is observed for  $\rho'_3 \geq 4$ .

In the following sections, the influence of the fracture shapes and of the permeability exponent  $\beta$  will be investigated, in order to see if they fit into this general model. However, it might be useful to first check the influence of a

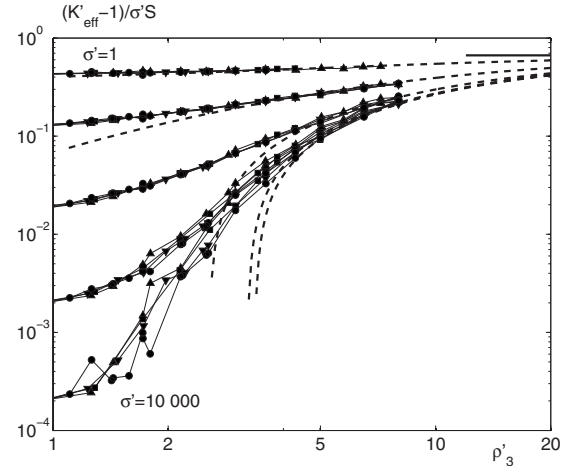


FIG. 14. The normalized mean permeability increments  $(K'_{\text{eff}} - 1)/\sigma' S$  for permeable media containing hexagonal fractures as functions of  $\rho'_3$ . Same numerical data as in Fig. 12. The broken lines correspond to the model (32).

parameter which has not been studied yet, namely the lower cutoff radius  $R'_m$ , i.e., the broadness of the fracture size distribution.

Recall that its influence on the network permeability  $K_n$  was shown by Mourzenko *et al.* [11] to be well described by the decomposition (13), for various size distributions including monodisperse; therefore, in view of (27) or (29), it is also incorporated in the two parameters  $S$  and  $\rho'_3$  when the network permeability dominates  $K_{\text{eff}}$ . A few additional examples are provided in Fig. 15.

First, data for nonpercolating monodisperse networks in the range  $\rho'_3 \leq 3$  are compared to those for  $a=1.5$  with  $R'_m = 1/10$ . Of course, this situation was not considered by Mourzenko *et al.* [11] since the resulting  $K_n$  is equal to zero; but, the results for  $K_{\text{eff}}$  are found in very good agreement. Then, a few networks with  $a=1.5$  or  $2.9$  were generated with  $R'_m = 1/20$ , and progressively modified by removing the smallest fractures, i.e., by increasing  $R'_m$  up to  $1/4$  and thereby decreasing  $\rho'_3$ . The permeabilities calculated with  $\sigma' = 10$  and  $10^4$  are seen in Fig. 15 to be very close to the values of  $\langle K'_{\text{eff}} \rangle$  calculated as a function of  $\rho'_3$  when  $R'_m$  is kept constant and equal to  $1/10$ . Finally, the permeabilities of percolating or nonpercolating networks directly built with  $R'_m = 1/4$  also agree with the mean values obtained with  $R'_m = 1/10$ , over the whole range  $\sigma' = 1 - 10^4$ .

## VII. INFLUENCE OF THE FRACTURE SHAPE

### A. Dilute networks

As for the hexagonal fractures discussed in Sec. VI B, dilute networks have been addressed for other fracture shapes by considering a single fracture in the unit cell  $\tau_0$  of the periodic medium. Again, the diagonal components of the resulting anisotropic permeability tensor have been averaged in order to obtain the value of  $K'_{\text{eff}}$  expected for a set of noninteracting, randomly and isotropically oriented fractures in an infinite medium. The following data have been ob-

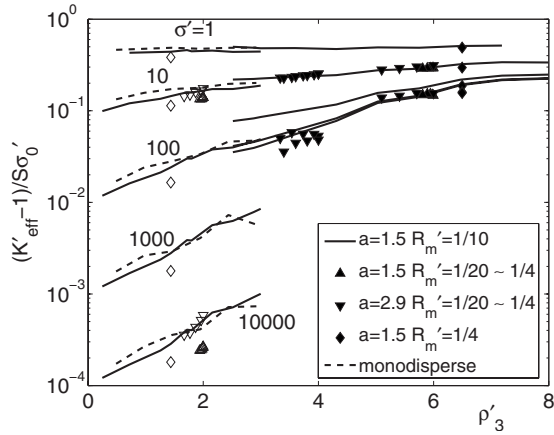


FIG. 15. The normalized mean permeability increments  $(K'_{\text{eff}} - 1)/\sigma' S$  for permeable media containing hexagonal fractures as functions of  $\rho'_3$ . The solid lines are data for  $a=1.5$  and  $R'_m=1/10$ , averaged over nonpercolating or percolating fracture networks, with  $\sigma' = 1 - 10^4$ . The broken lines are averages for nonpercolating monodisperse networks. The symbols correspond to individual realizations of networks with  $a=1.5$  ( $\Delta$ ) and  $2.9$  ( $\nabla$ ), where the smallest fractures are progressively suppressed which implies an increase of  $R'_m$  from  $1/20$  to  $1/4$ ; the symbols ( $\diamond$ ) correspond to networks directly generated with  $a=1.5$  and  $R'_m=1/4$ . Open and closed symbols correspond to nonpercolating and percolating networks, respectively.

tained with  $L'=6$ , but systematic calculations with  $L'=4$  and some with  $L'=8$  checked that this dilution is sufficient in order for the second-order term in (19) to have a negligible contribution to  $K'_{\text{eff}}$ .

A large variety of shapes has been considered, including regular polygons (triangles, squares, hexagons, icosagons), rectangles, and ellipses with aspect ratios 2, 4, and 8. These objects are isotropically distributed in space. The numerical errors induced by the discretization effects have been dealt with in the same way as for hexagons in Sec. VI B, i.e., the computations have been repeated with  $\delta'=1/4$ ,  $1/8$ , and  $1/16$ , and the data extrapolated toward  $\delta' \rightarrow 0$ .

An example is shown in Fig. 16 for very permeable fractures with  $\sigma'=10^4$ , which can be considered as a superconducting case, as seen in the following. The coefficient  $\kappa$  in the expansion (19) is plotted as a function of the shape factor  $v_{\text{ex}}/\pi^2$ , which decreases from one for disks to zero as the fracture shape becomes more irregular.

The discretization errors are large in some cases, especially for the most slender rectangles, but the extrapolation is successful in correcting them. The extrapolated values for ellipses are very close to the theoretical result (20b), and those for polygons are also close to the numerical data of Mansfield *et al.* [24], when available, i.e., for regular polygons with three to eight vertices. All the data presented in the rest of this section are obtained by the same extrapolation technique.

It can be noted that the dependence of  $\kappa$  for ellipses in (20b) on the aspect ratio suggests that the shape factor  $v_{\text{ex}}$  included in the definition of  $\rho'_3$  is not the most appropriate one in the general case for noninteracting fractures. However, as already noted about the results of Mansfield *et al.*

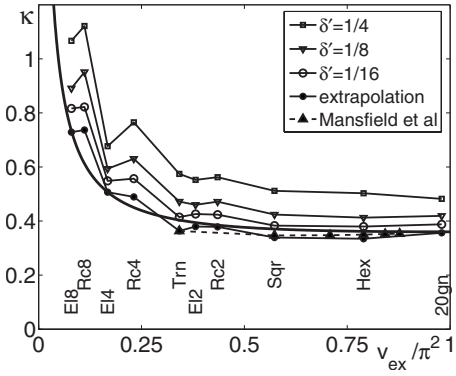


FIG. 16. The coefficient  $\kappa$  in Eq. (19) for dilute dispersions of fractures with various shapes, as a function of the shape factor  $v_{\text{ex}}/\pi^2$ . Data are for  $\delta'=1/4$  ( $\square$ ),  $1/8$  ( $\nabla$ ),  $1/16$  ( $\circ$ ), and  $0$  ( $\bullet$ , extrapolation),  $\sigma'=10^4$ . The solid line corresponds to the theoretical result (20b) for ellipses. The broken line joins the data ( $\Delta$ ) of Mansfield *et al.* [24] for regular polygons.

[24],  $\kappa$  varies very little over the range  $0.3 \leq v_{\text{ex}}/\pi^2 \leq 1$ , which covers the elongated rectangles or ellipses with aspect ratios up to 3. Hence, for most practical applications, the value  $\kappa \approx 0.36$  for disks [see Eq. (20a)] can be applied with a relative error smaller than a few percent. Therefore, it is possible and desirable in view of its prominent role in the other regimes to use  $\rho'_3$  to quantify the fracture density in this regime as well. For very slender shapes, a very good approximation can be obtained by using the expression (20b).

Data for less permeable fractures, with  $\sigma'=1$  to  $10^4$ , are shown in Fig. 17. There is little difference between the results for all the values of  $\sigma' \geq 100$ , but the coefficient  $\kappa$  noticeably decreases for smaller values, and especially for the most slender fracture shapes. The range where the value of  $\kappa$  for disks can be reasonably applied widens and progressively encompasses more and more elongated fracture shapes.

Therefore, for practical purposes,  $\kappa$  can be fairly accurately estimated by the heuristic formula (24) which was proposed for hexagons, in a range  $0.3 \leq v_{\text{ex}}/\pi^2 \leq 1$  for very con-

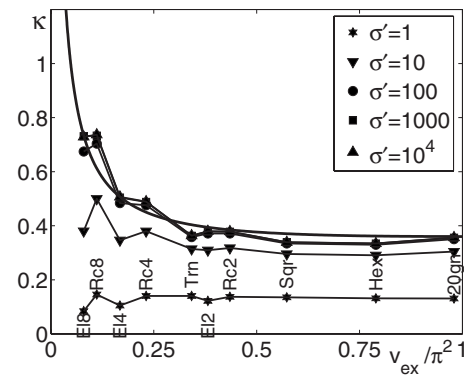


FIG. 17. The coefficient  $\kappa$  in Eq. (19) for dilute dispersions of fractures with various shapes, as a function of the shape factor  $v_{\text{ex}}/\pi^2$ . The data are extrapolations toward  $\delta' \rightarrow 0$ , when  $\sigma'=1$  ( $\star$ ),  $10$  ( $\nabla$ ),  $10^2$  ( $\bullet$ ),  $10^3$  ( $\square$ ), and  $10^4$  ( $\Delta$ ). The solid line corresponds to the theoretical result (20b) for very conducting ellipses.

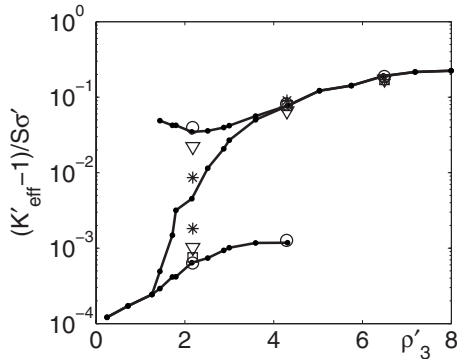


FIG. 18. The normalized mean permeability increments  $(K'_{\text{eff}} - 1)/\sigma' S$  for permeable media containing fractures of various shapes, as functions of  $\rho'_3$ . Data are for  $a=1.5$ ,  $\sigma'=10^4$ , and  $R'_m=0.1$ . The symbols correspond to triangle ( $\nabla$ ), squares ( $\square$ ), rectangles with an aspect ratio of 4 ( $\star$ ), and icosagons ( $\circ$ ). The curves correspond to the numerical data for hexagonal fractures. When applicable, the averages are taken separately for percolating and nonpercolating networks.

ducting fractures, or even wider when they are less permeable.

### B. Dense networks

The influence of the fracture geometry for dense networks is investigated by considering regular triangles, squares, and icosagons (20-gons), as well as rectangles with an aspect ratio of 4. In all cases, the fracture size is quantified by the radius  $R$  of their circumscribed circle.

A set of data for  $a=1.5$  is compared in Fig. 18 to the corresponding results for hexagonal fractures. In each case, 10 realizations are considered, and the effective permeability is calculated over the three directions  $x$ ,  $y$ , and  $z$ . The reported data are the averages of the 30 resulting values, or separately over the cases of percolating and nonpercolating networks, when applicable. Three densities  $\rho'_3=2.2, 4.3$ , and  $6.5$  are tested, and the conductivity  $\sigma'$  is varied from 1 to  $10^4$ . Only the results for  $\sigma'=10^4$  are reported, since for this value the fracture shape is expected to have the largest influence.

The data in Fig. 18 are expressed in terms of the normalized permeability increment  $(K'_{\text{eff}} - 1)/\sigma' S$ , since it is the quantity which is expected to depend only on  $\rho'_3$ , according to Eq. (27). This is indeed perfectly verified for all the fracture shapes when  $\rho'_3 > 4$ .

In the transition region for  $\rho'_3=2.2$ , it is also verified for squares and icosagons. However, the data for rectangles and in a lesser respect for triangles deviate more from the results for hexagons. This is not surprising, for two reasons. First, the discretization errors are maximum in this range and they should influence the two shapes which are the most departing from circularity since they originate at the fractures edges. Second, Mourzenko *et al.* [10] showed that the finite size effects, which are significant in this range of density, depend on the fracture shape.

Other values of the parameters were studied. Data for squares are shown in Fig. 19, obtained under the same con-

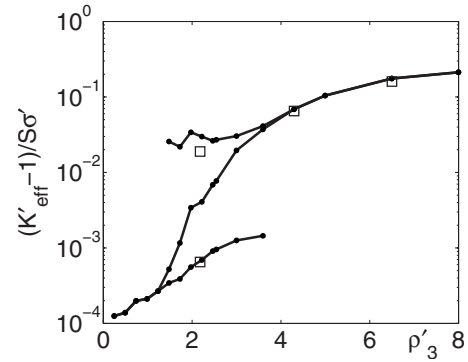


FIG. 19. The normalized mean permeability increments  $(K'_{\text{eff}} - 1)/\sigma' S$  for permeable media containing square ( $\square$ ) or hexagonal (lines) fractures, as functions of  $\rho'_3$ . Data are for  $a=2.5$ ,  $\sigma'=10^4$ , and  $R'_m=0.1$ . When applicable, the averages are taken separately for percolating and nonpercolating networks.

ditions with  $a=2.5$ ; they are also found in perfect agreement with those for hexagons. The same comments apply for smaller values of  $\sigma'$  (not displayed), for  $a=1.5$  and  $2.5$ , except that the deviations in the transition zone decrease. Therefore, (27) indeed accounts for the effect of the shape of very conducting fractures, and in addition, its extension (29) with (32) also applies when  $\sigma'$  is small or moderate.

## VIII. INFLUENCE OF THE PERMEABILITY EXPONENT $\beta$

In this brief section, a few illustrative results are provided for size-dependent fracture permeabilities. Only dense networks of hexagonal fractures are considered, since in the dilute limit the contributions of the individual fractures are independent. Therefore, at least to first order, the influence of  $\beta$  can be accounted for by generalizing Eq. (24) as

$$\kappa = \left\langle \frac{\sigma'(R)}{\sigma'(R) + 3/2} \right\rangle \kappa_{\infty}. \quad (33)$$

The exponent  $\beta$  was set to 1.5, 3, and 6, which are the values previously investigated by Mourzenko *et al.* [11] when studying the network permeability  $K_n$ . The data displayed in Fig. 20 are the permeabilities averaged over the three directions in 24 random realizations, with  $a=1.5$ ,  $R'_m=0.1$ , and  $\sigma'_0=1-10^4$ .

First, the permeability increments  $K'_{\text{eff}} - 1$  are displayed in Fig. 20(a). They are seen to decrease when  $\beta$  increases, which is expected since the fracture permeabilities become smaller and smaller [see Eq. (10)]. Then, the same data are plotted in Fig. 20(b), in the form of  $(K'_{\text{eff}} - 1)/\sigma' S$ . The weighted volumetric area  $S$  incorporates a contribution of  $\beta$  [see Eq. (17)], through the ponderation by  $\sigma(R)$  of the fracture areas. This normalization is seen to unify the results for all the values of the exponent  $\beta$ . The data for the extreme case  $\beta=6$  when  $\sigma'_0=10^4$  are slightly smaller, by a factor of about 2/3, but this is a very small difference when compared to the ratio of 1/10 in the corresponding cases in Fig. 20(a).

The same kind of calculations with an exponent  $a=2.5$  yield very similar results, which are not displayed here. In-

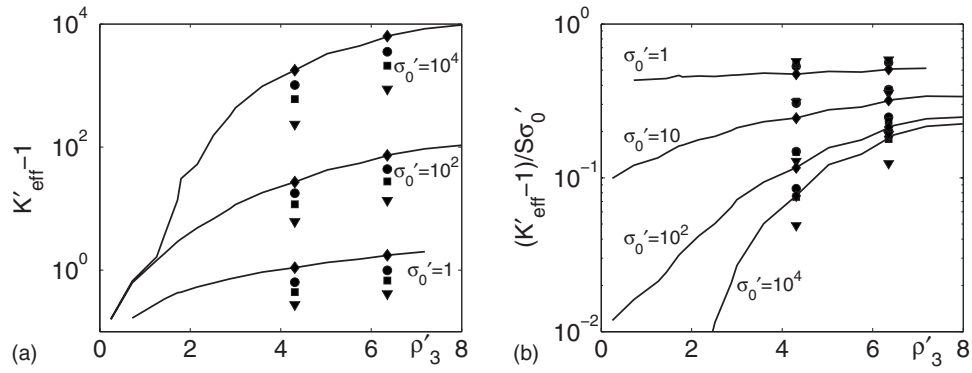


FIG. 20. The mean permeability increments  $K'_{\text{eff}}-1$  (a) and  $(K'_{\text{eff}}-1)/\sigma'_0 S$  (b) for media containing hexagonal fractures, as functions of  $\rho'_3$ . Data are for  $a=1.5$ ,  $R'_m=0.1$ , and  $\sigma'_0=1-10^4$ . The symbols correspond to  $\beta=0$  ( $\diamond$ ), 1.5 ( $\circ$ ), 3 ( $\square$ ) or 6 ( $\nabla$ ). The curves are the results for  $\beta=0$ .

stead, the ratio  $\omega$  [see Eq. (30)] for all the available data is shown in Fig. 21, as a function of  $\sigma'_0$ . All the data of Fig. 20 for  $a=1.5$  are shown, together with additional ones for other values of  $\sigma'_0$ , and a full set of data obtained in the same conditions with  $a=2.5$ .

The data are more scattered around the model (31) than for  $\beta=0$  in Fig. 13, with deviations of the order of  $\pm 0.1$ , but this corresponds to relative errors smaller than 20% for  $\sigma'_0 \geq 10$  and smaller than 10% for  $\sigma'_0 \geq 10^2$ . Part of the deviations for small  $\sigma'_0$  may originate in round-off errors, since the permeability  $\sigma'$  of the smallest fractures is very small. Recall also that for fracture networks in impermeable materials, Mourzenko *et al.* [11] found that Eq. (13) cannot be applied when both exponents  $a$  and  $\beta$  are large, and that this feature probably applies to  $K_{\text{eff}}$  as well.

With this reservation, and all due caution in view of the limited number of investigated cases, we may conclude that  $\mathcal{S}$  in Eq. (27) satisfactorily accounts for the influence of the exponent  $\beta$  on the macroscopic effective permeability. This also applies to the extension [(29) and (32)] of this model.

## IX. CONCLUSION

The effective macroscopic permeability of fractured porous media has been investigated numerically for a wide

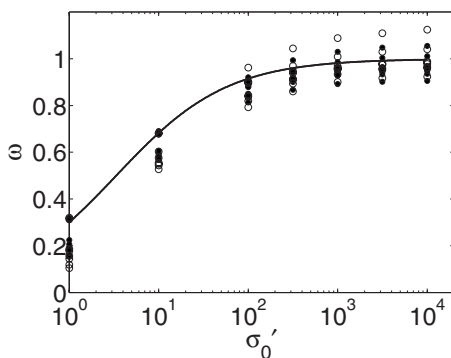


FIG. 21. The ratio  $\omega$  [see Eq. (30)] as a function of  $\sigma'_0$ . Data are for  $a=1.5$  ( $\bullet$ ), including all the data of Fig. 20 and additional ones for other values of  $\sigma'_0$ , and for a similar set of results with  $a=2.5$  ( $\circ$ ). The solid line is the model (31).

range of parameters which include the fracture density, shape and size distribution, and the permeability, possibly size dependent, of the fractures.

The results have been discussed and rationalized in terms of the two parameters  $\rho'_3$  (5) and  $\mathcal{S}$  (17). The former is a dimensionless measure of the density of fractures, which is known from earlier works to control the percolation and many other properties of the fracture networks, and which incorporates the influence in this respect of the fracture shape and size distribution. The latter is a measure of the volumetric area of fractures in the medium, weighted by the individual permeabilities, and can thereby account for their size dependence.

Unified models could be proposed in two regimes, which fit fairly well the numerical data throughout the investigated range of the parameters, except for very elongated fracture shapes and for extreme dependences of the fracture permeability on their size.

For loose networks, which do not percolate, the macroscopic effective permeability  $K'_{\text{eff}}$  can be estimated by the quadratic expansion (25), where the coefficient  $\kappa$  can be obtained from the heuristic formula (24) and from its value (20a) for superconducting circular fractures.

For dense networks, when percolation is nearly certain,  $K'_{\text{eff}}$  is given instead by the general expression (29), where  $K''_2$  can be obtained from the heuristic formulas (28) and (32).

The intermediate transition range was less thoroughly investigated, but its width decreases as the domain size increases, and it ultimately vanishes for infinite media. Furthermore, it was shown that except for extremely permeable fractures, the percolation status does not significantly influence the average effective permeability.

Finally, it can be noted that the parameters  $R_m$ ,  $R_M$  and  $a$  of the fracture size distribution are embodied in the global quantities  $\rho'_3$  and  $\mathcal{S}$ , but do not appear explicitly in the models (25) or (30). Therefore, these models can be expected to apply for other types of size distribution function.

This work could be extended in many ways and the most interesting path certainly consists in modeling more precisely real systems. As already mentioned, the first important property is the heterogeneity of the porous matrix which was assumed to be constant in this paper; in real systems, matrix

porosities and permeabilities are distributed. Two types of media can be easily generated, namely correlated or layered media. Therefore, interesting interactions between various length scales are expected.

Another extension closely related to the previous ones concerns the spatial distribution of fractures which tend to grow cooperatively leading to strongly correlated structures [20]. Moreover, again because of their generation under stresses, fractures are not usually isotropically distributed.

This feature which has already been addressed in [15], should yield interesting extensions of these properties.

#### ACKNOWLEDGMENT

Most computations were performed at CINES (subsidized by the MENESR), whose support is gratefully acknowledged.

- 
- [1] M. Sahimi, *Flow and Transport in Porous Media and Fractured Rock* (VCH, New York, 1995).
- [2] P. M. Adler and J.-F. Thovert, *Fractures and Fracture Networks* (Kluwer Academic, Dordrecht, 1999).
- [3] National Research Council. *Conceptual Models of Flow and Transport in the Fractured Vadose Zone* (National Academy Press, Washington, D.C., 2001).
- [4] B. Berkowitz, *Adv. Water Resour.* **25**, 861 (2002).
- [5] O. Huseby, J.-F. Thovert, and P. M. Adler, *J. Phys. A* **30**, 1415 (1997).
- [6] N. Koudina, R. Gonzalez Garcia, J.-F. Thovert, and P. M. Adler, *Phys. Rev. E* **57**, 4466 (1998).
- [7] I. I. Bogdanov, V. V. Mourzenko, J.-F. Thovert, and P. M. Adler, *Water Resour. Res.* **39**, 1023 (2003).
- [8] I. I. Bogdanov, V. V. Mourzenko, J.-F. Thovert, and P. M. Adler, *Water Resour. Res.* **39**, 1, 1021 (2003).
- [9] I. I. Bogdanov, V. V. Mourzenko, J.-F. Thovert, and P. M. Adler, *Phys. Rev. E* **68**, 026703 (2003).
- [10] V. V. Mourzenko, J.-F. Thovert, and P. M. Adler, *Phys. Rev. E* **72**, 036103 (2005).
- [11] V. V. Mourzenko, J.-F. Thovert, and P. M. Adler, *Phys. Rev. E* **69**, 066307 (2004).
- [12] E. Bonnet, O. Bour, N. E. Odling, P. Davy, I. Main, P. Cowie, and B. Berkowitz, *Rev. Geophys.* **39**, 347 (2001).
- [13] A. Bensoussan, J.-L. Lions, and G. Papanicolaou, *Asymptotic Analysis for Periodic Structures* (North-Holland, Amsterdam, 1978).
- [14] I. Balberg, C. H. Anderson, S. Alexander, and N. Wagner, *Phys. Rev. B* **30**, 3933 (1984).
- [15] M. Masihi, P. R. King, and P. Nurafza, *Phys. Rev. E* **74**, 042102 (2006).
- [16] M. Madadi and M. Sahimi, *Phys. Rev. E* **67**, 026309 (2003).
- [17] Y. Meheust and J. Schmittbuhl, *Geophys. Res. Lett.* **27**, 2989 (2000).
- [18] Y. Meheust and J. Schmittbuhl, *Pure Appl. Geophys.* **160**, 1023 (2003).
- [19] V. Mourzenko, J.-F. Thovert, and P. M. Adler, *Transp. Porous Media* **45**, 89 (2001).
- [20] M. Belayneh, M. Masihi, S. K. Matthai, and P. R. King, *J. Geophys. Eng.* **3**, 219 (2006).
- [21] J. C. Maxwell, *Electricity and Magnetism* (Clarendon, Cambridge, 1873).
- [22] B. Shafiro and M. Kachanov, *J. Appl. Phys.* **87**, 8561 (2000).
- [23] H. S. Carslaw and J. C. Jaeger, *Conduction of Heat in Solids* (Oxford University Press, Oxford, 1959).
- [24] M. L. Mansfield, J. F. Douglas, and E. J. Garboczi, *Phys. Rev. E* **64**, 061401 (2001).
- [25] D. T. Snow, *Water Resour. Res.* **5**, 1273 (1969).
- [26] S. Sisavath, V. V. Mourzenko, P. Genthon, J. F. Thovert, and P. M. Adler, *Geophys. J. Int.* **157**, 917 (2004).
- [27] S. Kirkpatrick, *Phys. Rev. Lett.* **27**, 1722 (1971).
- [28] D. Stauffer and A. Aharony, *Introduction to Percolation Theory*, 2nd ed. (Taylor and Francis, Bristol, 1994).